

pubs.acs.org/cm Article

Rb₂Sn₄Q₉ (Q = S and Se): Low-Dimensional Noncentrosymmetric Chalcogenides with High Laser-Induced Damage Threshold

Abishek K. Iyer, Seung Heon Ha, Michael J. Waters, Thomas S. Ie, Seung Han Shin, James M. Rondinelli, J. I. Jang,* and Mercouri G. Kanatzidis*



Cite This: Chem. Mater. 2023, 35, 8706-8713



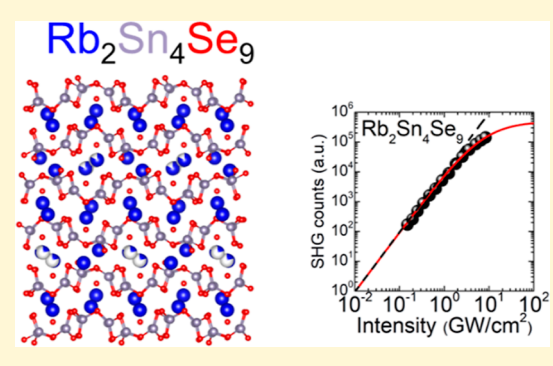
ACCESS I

III Metrics & More

Article Recommendations

s Supporting Information

ABSTRACT: Low-dimensional chalcogenides have shown promising non-linear optical (NLO) responses in the infrared region. Rb₂Sn₄Q₉ (Q = S and Se) crystallizes in the noncentrosymmetric orthorhombic space group $P2_12_12_1$. These compounds comprise an anionic layer of $[Sn_4Q_9]^{2-}$ chains separated by the Rb atoms located between the layers. Differential thermal analysis shows that Rb₂Sn₄Se₉ melts congruently, having a melting point temperature of 472 °C and a crystallization temperature of 443 °C and no observable phase transitions, making them promising for large crystal growth. These compounds' air- and water-stability make them more viable for application compared to the challenges faced in other promising NLO materials like γ -NaAsSe₂. The Rb₂Sn₄S₉ and Rb₂Sn₄Se₉ have energy band gaps of 2.56 and 1.75 eV, respectively. Second harmonic generation from



 $Rb_2Sn_4Q_9$ was found to be nonphase matchable for particle size above 75 μ m, with $Rb_2Sn_4Se_9$ having a $\chi^{(2)} = 36.7 \pm 7.4$ pm/V at 1800 nm. Both materials show a high laser-induced damage threshold (LIDT) of 1.8 GW/cm² and 0.2 GW/cm² for the sulfide and selenide compounds, respectively, which are significantly larger than that of the benchmark reference material, $AgGaSe_2$ (0.1 GW/cm²). The high LIDT values make these materials promising for NLO applications involving intense light—matter interactions.

■ INTRODUCTION

Nonlinear optical (NLO) materials play a crucial role in various applications due to their ability to manipulate light in unconventional ways. They are essential in fields such as telecommunications, laser technology, optical computing, and biophotonics, enabling functionalities such as frequency conversion, optical switching, signal processing, and imaging. Developing efficient and versatile NLO materials is vital for advancing these technologies and expanding their practical applications. 1-5 For a material to be suitable for NLO applications, it must possess certain characteristics, such as a noncentrosymmetric (NC) structure, high second-harmonicgeneration (SHG) intensity, a strong resistance to laserinduced damage, moderate birefringence, and the ability to melt congruently.^{6,7} NC oxides such as LiNbO₃, KH₂PO₄, and β -BaB₂O₄ have been extensively explored and commercialized in ultraviolet and visible regions. ⁸⁻¹⁰ However, oxides absorb in the infrared (IR) region, rendering their use in the mid-IR $(2-20 \mu m)$ region. Chalcogenides (Q = S, Se, and Te), on the other hand, exhibit transparency in the IR region, making them highly desirable for laser applications in the mid-IR range. Despite the commercial usage of AgGaS2 and AgGaSe2 as chalcogenides, their low band gaps and vulnerability to low laser-induced damage thresholds (LIDT) pose limitations in their performance. 11-13

Several reviews in the literature have discussed the existence of NC chalcogenide structural prototypes, encompassing zerodimensional (0D) to three-dimensional (3D) configurations. 6,7,14-16 NC structures are dominated by 3D structures $(\sim 70\%)$ primarily belonging to the chalcopyrite, for example, AgGaSe₂ and the $RE_3MM'Q_7$ family.^{7,17,18} In general, 3D chalcogenides with wide band gaps demonstrate high LIDT, yet their SHG response is often lower compared to the less explored low-dimensional chalcogenides. 19 However, these low-dimensional chalcogenides show significant promise, exhibiting higher SHG responses when compared with their 3D counterparts. Song et al.²⁰ studied the electronic structures of $AAsQ_2$ (A = alkali-metals; Li, Na, and K; Q = S and Se), a family of low-dimensional compounds characterized by $1D^{1}/_{\infty}[AsQ_{2}^{-}]$ chains. Experimentally, we uncovered an increased anisotropy in the materials with an increased interchain distance from β-LiAsS₂ to Na_{0.2}K_{0.8}AsSe₂.^{21,22} These materials show a high SHG response, with γ-NaAsSe₂ exhibiting an SHG susceptibility of $d_{11} = 590 \text{ pm V}^{-1}$ for single

Received: August 5, 2023 Revised: September 19, 2023 Published: October 6, 2023





crystal and β -LiAsS₂ having an SHG response \sim 10× that of AgGaSe2. Similarly, other low-dimensional materials like $Na_2Ge_2Se_5$ $(d_{eff} = 290 \text{ pm/V})^{23}$ and KPSe₆ $(d_{eff} = 157 \text{ pm/})^{23}$ V)^{24,25} have shown promise as IR NLO materials. Nonetheless, these materials suffer from problems like a phase transition in γ -NaAsSe₂ to centrosymmetric β -NaAsSe₂, β -LiAsSe₂ to centrosymmetric α-LiAsSe₂ or crystalline to amorphous phase transition in KPSe6. Phase transitions complicate the growth of large single crystals, which is one of the essential requirements for practical NLO applications. We recently reported that the stabilization of γ-NaAsSe₂ by Sb-doping resulted in \sim 3 mm \times 2 mm crystal dimensions of γ -NaAs_{0.95}Sb_{0.05}Se₂, showing the highest SHG response among materials with a band gap greater than 1.5 eV with a $d_{11} = 648$ pm/V.²⁶ Similarly, the stabilization of β -LiAsSe₂ by substituting Se with S resulted in LiAsSSe with a $d_{\text{eff}} = 410 \text{ pm/V.}^{27}$ However, these materials suffer from reactivity with water, resulting in challenges in polishing and obtaining high-quality crystals.

In this study, we present the investigation of low-dimensional materials, namely, $Rb_2Sn_4Q_9$ (where Q=S and Se). The structures of these compounds consist of layers containing $[Sn_4Q_9]^{2-}$ chains separated by Rb atoms. These materials show a band gap comparable to the commercial IR material $AgGaQ_2$, making them attractive for the study of their NLO properties. Notably, $Rb_2Sn_4Se_9$ demonstrates a SHG response comparable to $AgGaS_2$, while also exhibiting a higher LIDT than $AgGaQ_2$. These materials melt congruently, making them promising for single crystal growth essential for NLO applications.

■ EXPERIMENTAL SECTION

Starting Materials. All manipulations were performed under a dry nitrogen atmosphere in a glovebox. Commercially available Rubidium (Rb, Alfa Aesar, 99.95%), tin (Sn, Alfa Aesar, 99.9%), sulfur (S, Alfa Aesar, 99.5%), and selenium (Se, American elements, 99.999%) were used without further purification. Rb₂S and Rb₂Se were synthesized using the previously reported method. 28

Synthesis of Rb₂Sn₄Se₉. Rb₂Se (0.737 mmol), Sn (2.94 mmol), and Se (5.89 mmol) were ground thoroughly inside the glovebox and were loaded in a carbon-coated fused silica ampule. The tube was then flame-sealed under a vacuum (~3 × 10⁻³ mbar) and inserted in a programmable tube furnace. The temperature was increased to 750 °C in 10 h, annealed at 750 °C for 24 h, and cooled to 350 °C over 24 h to obtain a polycrystalline product. Grinding the sample resulted in a red powder of Rb₂Sn₄Se₉. Figure 1 shows the phase pure experimental powder X-ray diffraction (PXRD) pattern for Rb₂Sn₄Se₉. Figure S1a.b confirms that SEM/EDS performed on a single crystal of the compound yielded the compositions Rb₂Sn₄S₉ and Rb₂Sn₄Se₉. Attempts to grow large crystals were made by slow cooling from 750

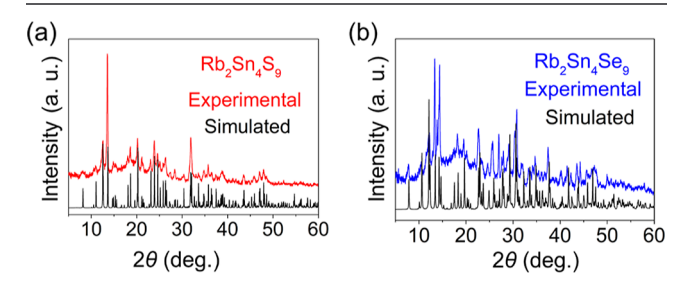


Figure 1. Experimental powder XRD patterns (a) $Rb_2Sn_4S_9$ (red) to the simulated pattern of $Rb_2Sn_4S_9$ obtained from single-crystal XRD and (b) $Rb_2Sn_4Se_9$ (blue) compared to the simulated pattern of $Rb_2Sn_4Se_9$ obtained from single-crystal XRD.

to 350 °C in 72 h, but the quality of crystals obtained was poor. The synthesis of Rb₂Sn₄S₉ can be found elsewhere, as reported by Marking et al.²⁹ Both compounds were observed to be air stable for more than 1 month and stable in water for over 2 days. The powder XRD of Rb₂Sn₄Se₉ is shown in Figure S2, showing no change in both air and water. The obtained yield for Rb₂Sn₄Se₉ based on Se was found to be 88%.

Crystal Characterization. X-ray powder diffraction patterns were collected on a Rigaku Miniflex600 diffractometer using Cu K α 1 radiation (λ = 0.154593 nm) equipped with a high-speed silicon strip detector. Finely powdered samples were measured on a flat, zero-background Si sample. The observed patterns were compared to simulated patterns based on the experimental CIF files.

Single-crystal X-ray diffraction: Plate-like crystals were chosen for the single-crystal X-ray diffraction study. Data were collected at 293 K using a STOE STADIVARI diffraction system with graded multilayer mirror monochromator Ag K α radiation operating at 50 kV and 40 mA with a Pilatus300 K CdTe detector. Individual frames were collected with scan widths of 1.0° in ω and 15 min exposure time. The X-AREA, X-RED, and X-SHAPE software packages were used for data extraction and integration and to apply analytical absorption corrections. In addition, direct methods and full-matrix least-squares refinement against F^2 were performed with the SHELXTL/2018 package. Table 1 summarizes the crystallographic details of Rb2Sn4Se9, and the atomic coordinates are listed in Table 2. The atomic displacement parameters and selected bond lengths are given in Tables S1 and S2.

Theoretical Density Functional Theory-Based SHG Calculations. All density functional theory (DFT) calculations were performed using the Perdew-Burke-Ernzerhof functional using the GPAW package version (22.8.1b1). For self-consistent calculations,

Table 1. Crystal Data and Structure Refinement for Rb₂Sn₄Se₉ at 293 K^a

empirical formula	$\mathrm{Rb_2Sn_4Se_9}$
formula weight	1356.34
temperature	300 K
wavelength	0.56083 Å
crystal system	Orthorhombic
space group	P2 ₁ 2 ₁ 2 ₁
unit cell dimensions	$a = 12.369(3) \text{ Å}, \alpha = 90^{\circ}$
	$b = 12.407(3) \text{ Å}, \beta = 90^{\circ}$
	$c = 26.284(5) \text{ Å}, \gamma = 90^{\circ}$
volume	4033.2(14) Å ³
Z	8
density (calculated)	4.464 g/cm^3
absorption coefficient	13.679 mm ⁻¹
F(000)	4637
crystal size	$0.23 \times 0.19 \times 0.15 \text{ mm}^3$
heta range for data collection	1.781 to 28.492°
index ranges	$-19 \le h \le 20, -20 \le k \le 21, -24 \le l \le 44$
reflections collected	42 091
independent reflections	$17\ 663\ [R_{\rm int}=0.0457]$
completeness to θ = 19.664°	97.5%
refinement method	full-matrix least-squares on F^2
data/restraints/parameters	17663/0/284
goodness-of-fit	1.027
final R indices $[I > 2\sigma(I)]$	$R_{\rm obs} = 0.0743, \ wR_{\rm obs} = 0.1973$
R indices [all data]	$R_{\rm all} = 0.1241$, $wR_{\rm all} = 0.2376$
extinction coefficient	0.0019(2)
flack	0.037
largest diff. peak and hole	4.357 and -2.031 e·Å ⁻³

 ${}^{a}R = \Sigma ||F_{o}| - |F_{c}||/\Sigma |F_{o}|, \ wR = (\Sigma [w(|F_{o}|^{2} - |F_{c}|^{2})^{2}]/\Sigma [w(|F_{o}|^{4})])^{1/2}$ and $w = 1/[\sigma^{2}(F_{o}^{2}) + (0.1334P)^{2} + 11.0960P]$ where $P = (F_{o}^{2} + 2F_{c}^{2})/3$.

Table 2. Atomic Coordinates $(\times 10^4)$ and Equivalent Isotropic Displacement Parameters $(\mathring{A}^2 \times 10^3)$ for Rb₂Sn₄Se₉ at 293 K with Estimated Standard Deviations in Parentheses

label	\boldsymbol{x}	y	z	occupancy	$U_{ m eq}^{a}$
Rb(1)	-5675(3)	-3374(3)	-342(2)	1	54(1)
Rb(2)	666(3)	-3067(2)	2101(2)	1	54(1)
Rb(3)	-4389(3)	-2477(4)	2719(2)	1	70(2)
Rb(4)	-5870(30)	-8179(12)	238(10)	0.70(10)	106(7)
Rb(5)	-5490(80)	-8060(40)	213(14)	0.27(10)	88(18)
Sn(1)	-2324(2)	-6320(2)	1621(1)	1	41(1)
Sn(2)	824(2)	412(2)	1432(1)	1	36(1)
Sn(3)	-2189(2)	584(2)	1395(1)	1	34(1)
Sn(4)	-7159(2)	-4636(2)	1096(1)	1	39(1)
Sn(5)	-4193(2)	-4472(2)	1091(1)	1	38(1)
Sn(6)	2768(2)	-1520(2)	928(1)	1	43(1)
Sn(7)	-4034(2)	-1344(2)	856(1)	1	41(1)
Sn(8)	-9082(2)	-6539(2)	1597(1)	1	43(1)
Se(1)	-5727(2)	-3102(2)	1458(2)	1	36(1)
Se(2)	-617(2)	1892(2)	1045(1)	1	34(1)
Se(3)	-7578(3)	-5271(2)	1991(2)	1	41(1)
Se(4)	1580(2)	1799(2)	2060(2)	1	38(1)
Se(5)	2415(2)	-924(2)	1821(2)	1	39(1)
Se(6)	-2851(3)	190(2)	492(2)	1	40(1)
Se(7)	-10641(2)	-5591(2)	2044(2)	1	41(1)
Se(8)	-5712(2)	-972(2)	328(2)	1	37(1)
Se(9)	1542(3)	26(3)	547(2)	1	42(1)
Se(10)	-2910(3)	1943(2)	2044(2)	1	42(1)
Se(11)	-5627(3)	-5457(3)	578(2)	1	46(1)
Se(12)	-8566(3)	-6138(3)	704(2)	1	46(1)
Se(13)	-776(2)	-747(2)	1730(2)	1	40(1)
Se(14)	-8306(2)	-3183(2)	661(2)	1	40(1)
Se(15)	-3859(3)	-727(3)	1751(2)	1	46(1)
Se(16)	-2735(3)	-5986(3)	711(2)	1	51(1)
Se(17)	-3753(3)	-5044(3)	1996(2)	1	45(1)
Se(18)	-3100(3)	-3083(2)	600(2)	1	44(1)

 $^aU_{eq}$ is defined as one-third of the trace of the orthogonalized U_{ii} tensor.

the Brillouin zone was sampled with a $2 \times 2 \times 1$ k-point grid for a density of >16 000 k-points per reciprocal $Å^3$. Simulation preparation and postprocessing are performed with the atomic simulation environment (ASE) version 3.23.1.³⁰ We used an electronic convergence criterion of 10⁻⁵ eV for energy eigenvalue changes between electronic iterations in the calculations. A low plane-wave energy cutoff of 300 eV was used since optical properties were found to be insensitive to this parameter. For linear and NLO properties calculations, the number of empty bands was increased until the highest empty bands were 15 and 10 eV above the conduction band minimum. This approximately corresponds to 2× and 3× the number of occupied bands. For NLO properties calculations in the length gauge, the k-grid was doubled to $4 \times 4 \times 2$. The macroscopic dielectric tensor elements were taken from the inverted microscopic dielectric matrix (truncated to 20 eV) to include local field effects. Calculations of optical properties were performed with 20 meV broadening and a scissor shift of 0.6 eV to compensate for the difference between the DFT fundamental gap and the experimentally measured band gap.

Nonlinear Optical Measurements. Crystalline powders of Rb₂Sn₄Q₉ (Q = Sn and S) were used for NLO characterization. Samples were sieved with size ranges of <25, 25–53, 53–75, 75–106, 106–150, and >150 μ m to examine the phase-matching behavior of SHG, LIDT, and two-photon absorption (2PA) coefficient β of the samples. Each sample was sealed in a glass capillary tube and mounted on a homemade sample holder. The SHG efficiencies of the samples were compared with a reference material, AgGaSe₂, which is a benchmark NLO material in the IR region. Note here that the particle size ranges of the references were <20, 20–53, 53–75, 75–106, 106–

150, and >150 μ m, which are slightly different from those for the sample; however, this does not affect our NLO characterization.

The SHG measurements were carried out at room temperature using the input wavelength ($\lambda = 1800 \text{ nm}$) and intensity (0.47 GW/ cm²): Unfortunately, it was not possible to measure the mid-IR SHG because of the insufficient SHG counts that are comparable to the dark counts of our InGaAs-based IR detector. Nevertheless, we confirmed that sample damage at this intensity is insignificant. Coherent light with a wavelength of 1064 nm was initially produced using an EKSPLA PL-2250 series diode-pumped Nd:YAG laser with a pulse width of 30 ps and a repetition rate of 50 Hz to generate tunable pulses. The Nd: YAG laser pumped an EKSPLA Harmonics Unit (HU) H400, in which the input beam was frequency tripled by the series of three-wave mixing. The beam then entered an EKSPLA PG403-SH-DFG optical parametric oscillator (OPO) composed of four main parts: (i) a double-pass parametric generator, (ii) a singlepass parametric amplifier, (iii) a second-harmonic generator (SH), and (iv) a difference frequency generation (DFG) scheme. The output wavelength from the OPO used in our experiments was 1800 nm, deliberately selected to ensure that SHG (900 nm) occurs below the bandgap of both the samples and the reference. This implies that the bandgap absorption of SHG can be neglected in the $\chi^{(2)}$ measurement. Also, the LIDT experiment was performed at λ = 1064 nm, a typical wavelength for DFG to generate mid-IR. Since our samples and reference are optically transparent at 1064 nm, multiphoton absorption is the primary mechanism for laser-induced damage. The SHG signal was collected using a reflection geometry and a fiber-optic bundle coupled to a spectrometer equipped with a

CCD camera. The data collection time was 60 s. A detailed description of our laser and detection setup can be found elsewhere.³¹

RESULTS AND DISCUSSION

The synthesis of phase-pure $Rb_2Sn_4Q_9$ (where Q = S and Se) compounds was successfully achieved through heating at 750 °C. Previous reports by Marking et al. 29 described the thin and poor quality of the obtained Rb₂Sn₄S₉ crystals, which were further confirmed in this study and depicted in Figure S3a. Attempts to enhance crystal quality by modifying the temperature profile or utilizing a few salt flux combinations for the sulfide compound proved unsuccessful, as demonstrated in Figure S3b. While crystals of Rb₂Sn₄Se₉ exhibited improved stability compared to Rb₂Sn₄S₉, they remained brittle and displayed minimal enhancement in crystal quality even after a 4 day cooling period, as illustrated in Figure S3c,d. The layered structure of these materials presents challenges for growing high-quality crystals, and other methods such as minor doping will need to be explored for successful crystal growth. Furthermore, attempts to substitute Rb with Cs using a composition of " $Cs_{0.25}Rb_{1.75}Sn_4Se_9$ " and Se with Te using a composition of " $Rb_2Sn_4Se_{1.75}Te_{0.25}$ " did not result in the incorporation of Cs and Te, as confirmed by the absence of shifts in the PXRD (Figure S4a,b) and verified through EDS analysis. Cs₂Sn₄S₉ was reported by Marking et al. to be crystallizing in the centrosymmetric space group Pnma.²⁹

Rb₂Sn₄Se₉ is isostructural to the Rb₂Sn₄S₉ structure-type and crystallizes with a large asymmetric unit in the orthorhombic space group P2₁2₁2₁. It is made up of 30 independent crystallographic sites: 18 Se atoms, 8 Sn atoms, and 4 Rb atoms. Figure 2a shows the crystal structure of the Rb₂Sn₄Se₉ is a two-dimensional structure made up of an anionic layer of [Sn₄Se₉]²⁻ chains separated by the Rb atoms located between the layers. Figure 2b shows that the [Sn₄Se₉]²⁻ cluster is made up of two tetrahedra SnSe₄ units and two trigonal pyramidal SnSe₃ units connected via corner-sharing Se atoms. The Sn-Se bond lengths in one tetrahedron range from 2.48 to 2.58 and 2.53 to 2.67 Å in the other tetrahedron. The two trigonal pyramidal units have a narrow bond length variation from 2.53 to 2.57 Å. Figure 2c shows that two $[Sn_4Se_9]^{2-}$ are in phase and two highlighted in the black box are out of phase and related by a 21 screw-axis. The Rb atoms sit between the $[Sn_4Se_9]^{2-}$ chains with the nearest Rb-Se bond length of 3.56 Å for Rb1, Rb2, and Rb3, while Rb4 shows disorder with the nearest Rb-Se bond length of 3.91 Å.

Differential thermal analysis (DTA) of Rb₂Sn₄S₉ was reported by Marking et al. Rb₂Sn₄S₉ melts congruently and exhibits a melting temperature $(T_{\rm m})$ of 655 °C and a crystallization temperature (T_c) of 614 °C. In comparison, $Rb_2Sn_4Se_9$ exhibits a lower $T_m = 472$ °C and a $T_c = 443$ °C (Figure 3a), as determined by DTA experiments. The PXRD before and after DTA showed no difference, suggesting the congruent melting behavior of the compound (Figure 3b). In the DTA for Rb₂Sn₄Se₉, a small event is observed at 454 °C, suggesting a possible degradation or phase transition. We performed variable-temperature powder X-ray diffraction (VT-PXRD) and did not see any suggestion of phase transition or material degradation. VT-PXRD (Figure S5) confirms that the materials $T_{\rm m}$ (470 °C) and $T_{\rm c}$ (438 °C) are comparable to the values obtained using DTA. Congruently melting behavior is essential for pursuing crystal growth for practical NLO applications.

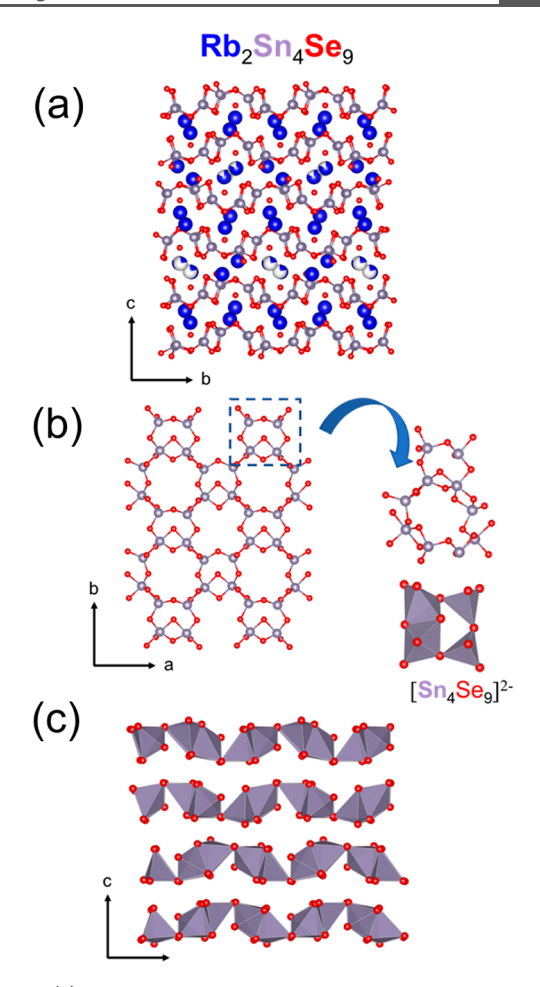


Figure 2. (a) Crystal structure of $Rb_2Sn_4Se_9$ showing the Rb atoms (blue) sandwiched between the $[Sn_4Se_9]^{2-}$ layers where Sn atoms are denoted in gray and the Se atoms denoted in red; (b) the Sn_4Se_9 chains made up of $SnSe_3$ and $SnSe_4$ units; (c) the arrangement of $SnSe_9$ chains showing the arrangement of the layers with the black box highlighting two out-of-phase layers.

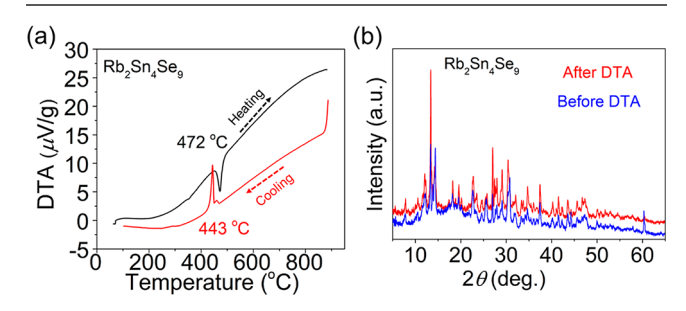


Figure 3. Differential thermal analysis of (a) $Rb_2Sn_4Se_9$ showing the melting (T_{mr} endothermic) and crystallizing (T_{cr} exothermic) points at 10 °C/min and (b) PXRD for $Rb_2Sn_4Se_9$ before DTA (blue) and after DTA (red).

Linear Optical Properties and Electronic Structure.

Figure 4 shows the solid-state optical absorption spectra for $Rb_2Sn_4Se_9$ and $Rb_2Sn_4S_9$ exhibiting band edges corresponding to the bandgaps (E_g) of 1.75 eV (red) and 2.56 eV (yellow), respectively. These bandgaps are consistent with the color of the materials dark red ($Rb_2Sn_4Se_9$) and yellow ($Rb_2Sn_4S_9$). These values are very close to the bandgaps of the benchmark $AgGaSe_2$ (1.83 eV) and $AgGaSe_2$ (2.66 eV) materials.

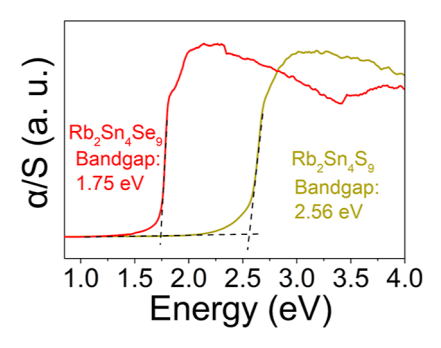


Figure 4. UV–visible optical absorption spectra of $Rb_2Sn_4Se_9$ (red) and $Rb_2Sn_4Se_9$ (yellow).

The obtained theoretical band gap for Rb₂Sn₄Se₉ was found to be 1.3 eV, which is underestimated owing to the use of semilocal exchange—correlation functionals. The experimental bandgap of Rb₂Sn₄Se₉ is also comparable to γ -NaAs_{0.95}Sb_{0.05}Se₂ ($E_{\rm g}=1.78$ eV), a material which was recently reported to show the highest SHG response ($d_{11}=648\pm74$ eV). γ -NaAs_{0.95}Sb_{0.05}Se₂ is the stabilized analogue of γ -NaAsSe₂, which is also a low-dimensional structure made up of 1D¹/ $_{\infty}$ [AsQ₂ $^{-}$] chains. Song et al. previously reported electronic structures of LiAsS₂ and γ -NaAsSe₂, showing that the combination of flat valence bands and high density of states contributes to the large $\chi^{(2)}$ in γ -NaAsSe₂. More recently, we reported that both γ -NaAsSe₂ and KAsSe₂ have flatter bands compared to LiAsS₂, but KAsSe₂ shows a much lower SHG response compared to both LiAsS₂ and γ -NaAsSe₂.

The calculated electronic band structure of Rb₂Sn₄Se₉ is shown in Figure 5, where the Se 3p states dominate the valence

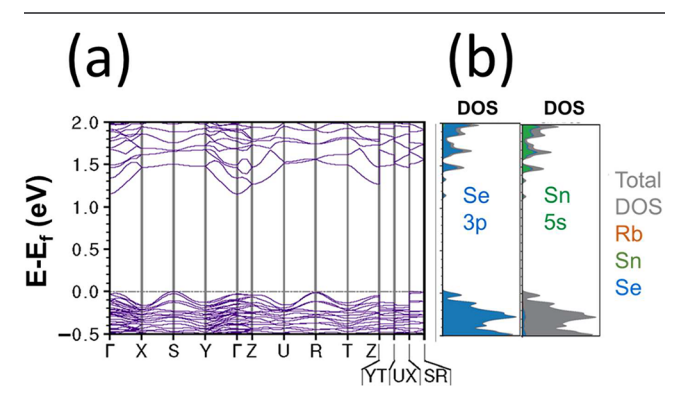


Figure 5. Calculated (a) band structure and (b) electronic density of states of Rb₂Sn₄Se₉

band (VB), while the Se 3p and a smaller contribution from Sn Ss states dominate the conduction band (CB). The band structure showed that Rb₂Sn₄Se₉ is an indirect semiconductor with a valence band maximum (VBM) at S and a conduction band minimum (CBM) at Γ . The long tail near the absorption edge in the experimental measurement for Rb₂Sn₄Se₉ also confirms that the material has an indirect band gap. We calculated the effective masses of holes for the VBM points S to X, Y, and R and electrons for the CBM points Γ to X, Y, and Z as shown in Table 3 to understand the flatness of the bands. For γ -NaAsSe₂ and KAsSe₂, we found that γ -NaAsSe₂ had much higher effective masses compared to KAsSe₂ and a higher SHG response. The calculated values of m_h^* are larger than m_e^* in all directions, suggesting the VB to be flatter than

Table 3. Effective Masses of Holes and Electrons in $Rb_2Sn_4Se_9$

m 1	ate.			
effective mass direction	m*			
holes (mh*)				
$S \to X$	$0.891 \ m_0$			
$S \rightarrow Y$	$0.956 \ m_0$			
$S \rightarrow R$	$7.535 \ m_0$			
electrons (m _e *)				
$\Gamma \to X$	$0.457 \ m_0$			
$\Gamma \to Y$	$0.382 \ m_0$			
$\Gamma \to Z$	$0.452 \ m_0$			

the CB. The very large value of m_h^* in the $S \rightarrow R$ direction reflects the fact that the bands are very flat in that direction.

NLO Properties. An efficient SHG process relies on the concept of phase-matching, where the phase velocities of the fundamental and SHG waves align to ensure constructive interference and efficient energy conversion. Understanding the phase-matchability of NLO materials and their wavelength-dependent characteristics is crucial for designing and optimizing NLO devices and applications. Phase-matchability is highly dependent on the wavelength of the incident light. Different materials have unique phase-matching characteristics, and they may exhibit phase-matchability in specific wavelength ranges while being nonphase-matchable in others. In Figure 6, size-dependent SHG counts are

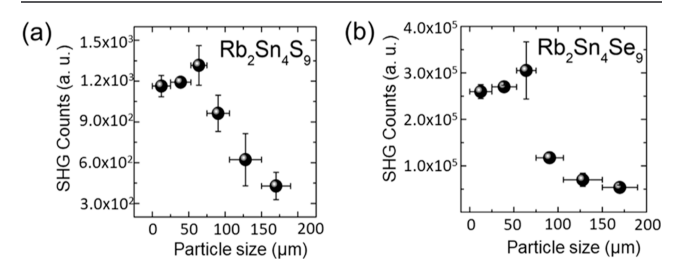


Figure 6. Particle size dependence of SHG for (a) $Rb_2Sn_4S_9$ and (b) $Rb_2Sn_4Se_9$ at $\lambda=1800$ nm. The experimental coherence lengths were determined to be 60 μ m, for $Rb_2Sn_4S_9$ and $Rb_2Sn_4Se_9$, respectively.

presented for the reported samples, Rb₂Sn₄S₉ (Figure 6a), and Rb₂Sn₄Se₉ (Figure 6b) at a wavelength of 1800 nm. As the particle size of both compounds increases from 20 to 60 μ m, the SHG counts show a gradual increase. However, beyond 60 um, the SHG counts start to decrease rapidly. This suggests that neither sample is phase-matchable at this particular wavelength, with a coherence length of 60 μ m. In comparison, the results for AgGaSe2 also indicate that it is not phasematchable at 1800 nm (Figure S6). In contrast, the coherence length of AgGaSe2 cannot be accessed experimentally as the SHG counts drop with increasing particle size from the smallest size range <20 μ m. Therefore, we estimated the coherence length for AgGaSe₂ to be about 15.0 μm using the relation, $l = \lambda/4\Delta n$, with Δn being the index mismatch based on the measured refractive indices for ordinary and extraordinary axes.35

Using the Kurtz powder method, the second-order susceptibility of each sample, $\chi_{\rm S}^{(2)}$, was calculated for the nonphase matching case 22,31

$$\chi_{\rm S}^{(2)} = \chi_{\rm R}^{(2)} \frac{l_{\rm R}}{l_{\rm S}} \left(\frac{I_{\rm S}^{\rm SHG}}{I_{\rm R}^{\rm SHG}} \right)^{1/2} \tag{1}$$

where $I_{\rm S}^{\rm SHG}$ and $I_{\rm R}^{\rm SHG}$ are the measured maximum SHG counts from the sample and the reference, and $l_{\rm S}$ and $l_{\rm R}$ are the experimental SHG coherence lengths of the sample and the reference, which were determined to be 15.0 μ m for AgGaSe₂ and 60 μ m for both Rb₂Sn₄S₉ and Rb₂Sn₄Se₉, respectively. Using $\chi_{\rm R}^{(2)} \sim 66$ pm/V for AgGaSe₂, ³⁵ our calculation yields $\chi_{\rm S}^{(2)}({\rm Rb_2Sn_4Se_9}) \sim 2.4 \pm 0.2$ pm/V and $\chi_{\rm S}^{(2)}({\rm Rb_2Sn_4Se_9}) \sim 36.7 \pm 7.4$ pm/V at $\lambda = 1800$ nm. The phase-matching properties of the title compounds are critically dependent on the birefringence. The linear optical responses for an orthorhombic anisotropic system can be obtained using the following equation, $\tilde{n} = n + ik$, where n is the refractive index and k is the extinction coefficient. The extinction coefficient increases once the photon energy exceeds the band gap (1.75 eV), as shown in Figure 7. The theoretical birefringence (Δn) of Rb₂Sn₄Se₉

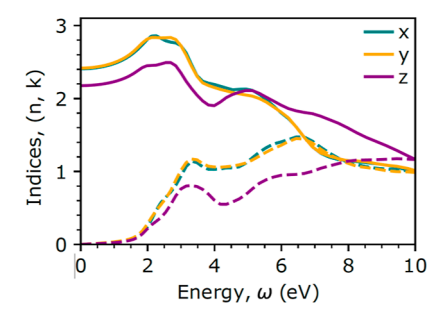


Figure 7. Theoretical dispersion curves obtained for the refractive indices of $Rb_2Sn_4Se_9$. The solid traces correspond to the refractive index (n) along the x-direction (blue), y-directions (orange), and z-directions (purple), and the dashed traces correspond to the imaginary part of the dielectric function, which is the extinction coefficient (k) along the x-direction (blue), y-directions (orange), and z-directions (purple), respectively.

was 0.10, as shown in Figure 7. The compound shows a crossover of $n_{x/}n_y$ and n_z near 5 eV, suggesting that the long coherence length (60 μ m) of Rb₂Sn₄Se₉ results in phase matchability at higher wavelengths.

For high-power laser systems, a material with a large LIDT is essential, and the use of $AgGaSe_2$ is greatly limited for high-power applications.³⁶ To determine the LIDT, we measured the SHG counts of $Rb_2Sn_4S_9$ and $Rb_2Sn_4Se_9$ powders with an average particle diameter range of $106-150~\mu m$. The measurements were performed at 1064~nm, as we varied the input intensity (refer to Figure 8). It is important to note that $Rb_2Sn_4S_9$ exhibits three-photon absorption (3PA) activity at

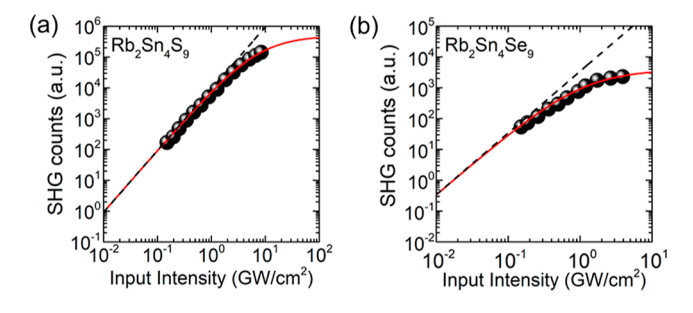


Figure 8. Logarithmic plots of the SHG counts versus input intensity of (a) Rb₂Sn₄S₉ and (b) Rb₂Sn₄Se₉ for I=0.1-10 GW/cm² at $\lambda=1064$ nm. The red curve indicates the best fit for each case using eqs 2 and 3. The black dashed line corresponds to the case of $\gamma=0$ for Rb₂Sn₄Se₉ and $\beta=0$ for Rb₂Sn₄Se₉.

this excitation wavelength, whereas $Rb_2Sn_4Se_9$ displays two-photon absorption (2PA) activity. The SHG counts, which are directly proportional to the SHG intensity, can be expressed as follows

$$I_{\text{SHG,2PA}} = a \left(\frac{I}{1 + Id\beta} \right)^2 \tag{2}$$

$$I_{\text{SHG,3PA}} = b \left(\frac{I^2}{1 + 2\gamma dI^2} \right) \tag{3}$$

where I is the fundamental input intensity, β is the 2PA coefficient, γ is the 3PA coefficient, d is the average particle size, and a and b are proportionality constants that incorporate $\chi^{(2)}$.³⁷ We estimated the LIDT as the SGH intensity in which the data (dots) deviate from the black line in Figure 8. Accordingly, LIDT and β of Rb₂Sn₄Se₉ are 0.3 GW/cm² and 51.4 cm/GW. For Rb₂Sn₄Se₉, LIDT and γ are each 1.8 GW/cm² and 0.15 cm³/GW². Generally, the LIDT of a compound is directly proportional to the band gap of the material, and this trend is also observed in the title compounds, with the larger bandgap sulfide showing a higher LIDT compared to the lower bandgap selenide.³⁸ Table 4 summarizes the measured NLO

Table 4. Comparison of NLO Properties of Samples and the Reference

	${\rm AgGaSe_2}$	$Rb_2Sn_4S_9$	$Rb_2Sn_4Se_9$
$\chi^{(2)} \; (\text{pm/V}) \; (1800 \; \text{nm})$	66	2.4 ± 0.2	36.7 ± 7.4
β (cm/GW) (1064 nm)	38 ³⁷	N/A	51.4 ± 1.3
$\gamma \text{ (cm}^3/\text{GW}^2) \text{ (1064 nm)}$	N/A	0.15 ± 0.01	N/A
LIDT (GW/cm^2) (1064 nm)	0.2^{31}	1.8 ± 0.3	0.3 ± 0.1
band gap (eV)	1.83	2.56	1.75

parameters of the title compounds. It should be noted that a direct LIDT comparison between different materials especially in the powder is difficult as LIDT is dependent on the spot-size, pulse-width, and the wavelength of the laser used. However, as suggested by Chen et al., factors like reduced anisotropy in a material can play a large role in the LIDT. The lower effective mass of Rb₂Sn₄Se₉ in comparison to γ -NaAsSe₂ suggests reduced anisotropy in Rb₂Sn₄Se₉, which could be attributed to the higher LIDT in the title compounds. More characterization of these materials will be required to understand the role played by the structure in enhancing the LIDT in low-dimensional materials.

CONCLUSIONS

The Rb₂Sn₄Se₉ compound adopts an orthorhombic space group $P2_12_12_1$, consisting of a two-dimensional anionic layer of $[Sn_4Se_9]^{2^-}$ separated by Rb atoms. The $[Sn_4Se_9]^{2^-}$ layer comprises two tetrahedral SnSe₄ units and two trigonal pyramidal SnSe₃ units connected via corner-sharing Se atoms. The melting point $(T_{\rm m})$ and crystallization temperature $(T_{\rm c})$ of Rb₂Sn₄Se₉ were determined to be 472 and 443 °C, respectively, exhibiting lower values compared to their sulfide counterparts. The band gaps of Rb₂Sn₄Se₉ and Rb₂Sn₄S₉ were found to be 1.75 and 2.56 eV, respectively, similar to those of benchmark materials AgGaSe₂ and AgGaS₂. Rb₂Sn₄Se₉ demonstrated an indirect band gap nature, with the Se 3p states dominating the valence band and the Se 3p and Sn 5s states contributing to the conduction band. The SHG response of Rb₂Sn₄Se₉ was measured, showing size-dependent behavior

to be nonphase-matching. The compounds exhibited a higher LIDT compared to AgGaSe₂, with LIDT values of 0.3 GW/cm² and 1.8 GW/cm² for Rb₂Sn₄Se₉ and Rb₂Sn₄S9, respectively. Overall, the obtained NLO parameters of Rb₂Sn₄Se₉ highlight its potential for mid-infrared NLO applications involving high-powered lasers (>1 kW), and the easy handling (air- and water-stability) of the materials makes them promising for crystal processing methods.

ASSOCIATED CONTENT

Supporting Information

The Supporting Information is available free of charge at https://pubs.acs.org/doi/10.1021/acs.chemmater.3c01962.

Experimental methods and physical property measurements; X-ray crystallographic tables of displacement parameters and selected bond lengths of $Rb_2Sn_4Se_9$; figures of energy dispersive spectroscopy data for $Rb_2Sn_4S_9$ and $Rb_2Sn_4Se_9$; PXRD patterns from all materials produced; optical images of materials produced for bulk reaction; variable temperature PXRD data for $Rb_2Sn_4Se_9$; and SHG intensity of $AgGaSe_2$. CSD number for $Rb_2Sn_4Se_9$: 2286965. (PDF)

AUTHOR INFORMATION

Corresponding Authors

J. I. Jang — Department of Physics, Sogang University, Mapogu, Seoul 04107, South Korea; orcid.org/0000-0002-1608-8321; Email: m-kanatzidis@northwestern.edu

Mercouri G. Kanatzidis — Department of Chemistry, Northwestern University, Evanston, Illinois 60208, United States; orcid.org/0000-0003-2037-4168; Email: jjcoupling@sogang.ac.kr

Authors

Abishek K. Iyer — Department of Chemistry, Northwestern University, Evanston, Illinois 60208, United States; orcid.org/0000-0002-8582-3895

Seung Heon Ha – Department of Physics, Sogang University, Mapo-gu, Seoul 04107, South Korea

Michael J. Waters — Department of Materials Science and Engineering, Northwestern University, Evanston, Illinois 60208, United States; orcid.org/0000-0001-6425-4331

Thomas S. Ie — Department of Chemistry, Northwestern University, Evanston, Illinois 60208, United States

Seung Han Shin – Department of Physics, Sogang University, Mapo-gu, Seoul 04107, South Korea

James M. Rondinelli — Department of Materials Science and Engineering, Northwestern University, Evanston, Illinois 60208, United States; orcid.org/0000-0003-0508-2175

Complete contact information is available at: https://pubs.acs.org/10.1021/acs.chemmater.3c01962

Notes

The authors declare no competing financial interest.

ACKNOWLEDGMENTS

We acknowledge partial support from the Air Force Office of Scientific Research Grant number FA9550-23-1-0658. This work was also supported in part by the National Science Foundation (DMR-2305731). The IMSERC PCM facility at Northwestern University used in this work received support

from the Soft and Hybrid Nanotechnology Experimental (SHyNE) Resource (NSF ECCS-2025633) and Northwestern University. Access to facilities for high-performance computing resources at Northwestern University and of the National Energy Research Scientific Computing Center, a DOE Office of Science User Facility supported by the Office of Science of the U.S. Department of Energy under Contract 477 No. DE-AC02-05CH11231 using NERSC award BES- 478 ERCAP0023827 are acknowledged. J.I.J. acknowledges the support of the Basic Science Research Programs (2021R1A2C2013625) and Basic Research Laboratory Program (2022R1S4S1033562) through the National Research Foundation of Korea (NRF), funded by the Korean government. T.S.I acknowledges the support from Materials Research Science and Engineering Centers (DMR-1720139 MRSEC).

REFERENCES

- (1) Serebryakov, V. A.; Boĭko, É. V.; Petrishchev, N. N.; Yan, A. V. Medical applications of mid-IR lasers. Problems and prospects. *J. Opt. Technol.* **2010**, *77* (1), 6–17.
- (2) Pushkarsky, M. B.; Dunayevskiy, I. G.; Prasanna, M.; Tsekoun, A. G.; Go, R.; Patel, C. K. High-sensitivity detection of TNT. *Proc. Natl. Acad. Sci. U.S.A.* **2006**, *103* (52), 19630–19634. From NLM
- (3) Schneider, T. Nonlinear Optics in Telecommunications; Springer Berlin: Heidelberg, 2004, pp 1–420.
- (4) Papadopoulos, M. G.; Sadlej, A. J.; Leszczynski, J. Non-linear Optical Properties of Matter; Springer, 2006.
- (5) Cotter, D.; Manning, R. J.; Blow, K. J.; Ellis, A. D.; Kelly, A. E.; Nesset, D.; Phillips, I. D.; Poustie, A. J.; Rogers, D. C. Nonlinear Optics for High-Speed Digital Information Processing. *Science* **1999**, 286 (5444), 1523–1528.
- (6) Chung, I.; Kanatzidis, M. G. Metal Chalcogenides: A Rich Source of Nonlinear Optical Materials. *Chem. Mater.* **2014**, 26 (1), 849–869.
- (7) Lin, H.; Wei, W.-B.; Chen, H.; Wu, X.-T.; Zhu, Q.-L. Rational design of infrared nonlinear optical chalcogenides by chemical substitution. *Coord. Chem. Rev.* **2020**, *406*, 213150.
- (8) Bierlein, J. D.; Vanherzeele, H. Potassium titanyl phosphate: properties and new applications. *J. Opt. Soc. Am. B* **1989**, *6* (4), 622–633.
- (9) Chen, C.; Sasaki, T.; Li, R.; Wu, Y.; Lin, Z.; Mori, Y.; Hu, Z.; Wang, J.; Aka, G.; Yoshimura, M. Nonlinear Optical Borate Crystals: Principals and Applications; John Wiley & Sons, 2012.
- (10) Boyd, G. D.; Miller, R. C.; Nassau, K.; Bond, W. L.; Savage, A. LiNbO3: An Efficient Phase Matchable Nonlinear Optical Material. *Appl. Phys. Lett.* **1964**, *5* (11), 234–236.
- (11) Catella, G. C.; Shiozawa, L. R.; Hietanen, J. R.; Eckardt, R. C.; Route, R. K.; Feigelson, R. S.; Cooper, D. G.; Marquardt, C. L. Mid-IR absorption in AgGaSe₂ optical parametric oscillator crystals. *Appl. Opt.* **1993**, 32 (21), 3948–3951.
- (12) Nikogosyan, D. N. Nonlinear Optical Crystals: A Complete Survey; Springer Science & Business Media, 2006.
- (13) Schunemann, P. Improved NLO Crystals for Mid-IR Laser Applications; SPIE, 2007.
- (14) Chen, H.; Ran, M.-Y.; Wei, W.-B.; Wu, X.-T.; Lin, H.; Zhu, Q.-L. A comprehensive review on metal chalcogenides with three-dimensional frameworks for infrared nonlinear optical applications. *Coord. Chem. Rev.* **2022**, *470*, 214706.
- (15) Ran, M.-Y.; Wang, A. Y.; Wei, W.-B.; Wu, X.-T.; Lin, H.; Zhu, Q.-L. Recent progress in the design of IR nonlinear optical materials by partial chemical substitution: Structural evolution and performance optimization. *Coord. Chem. Rev.* **2023**, *481*, 215059.
- (16) Abudurusuli, A.; Li, J.; Pan, S. A review on the recently developed promising infrared nonlinear optical materials. *Dalton Trans.* **2021**, *50* (9), 3155–3160.

- (17) Chen, H.; Wei, W.-B.; Lin, H.; Wu, X.-T. Transition-metal-based chalcogenides: A rich source of infrared nonlinear optical materials. *Coord. Chem. Rev.* **2021**, *448*, 214154.
- (18) Iyer, A. K.; Yin, W.; Rudyk, B. W.; Lin, X.; Nilges, T.; Mar, A. Metal ion displacements in noncentrosymmetric chalcogenides $La_3Ga_{1.67}S_7$, $La_3Ag_{0.6}GaCh_7$ (Ch = S, Se), and La_3MGaSe_7 (M = Zn, Cd). J. Solid State Chem. **2016**, 243, 221–231.
- (19) Akopov, G.; Hewage, N. W.; Viswanathan, G.; Yox, P.; Wu, K.; Kovnir, K. Non-Linear Optical Properties of the (RE)₃CuGeS₇ Family of Compounds. Z. Anorg. Allg. Chem. **2022**, 648 (15), No. e202200096.
- (20) Song, J.-H.; Freeman, A. J.; Bera, T. K.; Chung, I.; Kanatzidis, M. G. First-principles prediction of an enhanced optical second-harmonic susceptibility of low-dimensional alkali-metal chalcogenides. *Phys. Rev. B* **2009**, *79* (24), 245203.
- (21) (a) Bera, T. K.; Jang, J. I.; Song, J.-H.; Malliakas, C. D.; Freeman, A. J.; Ketterson, J. B.; Kanatzidis, M. G. Soluble Semiconductors AAsSe₂ (A = Li, Na) with a Direct-Band-Gap and Strong Second Harmonic Generation: A Combined Experimental and Theoretical Study. *J. Am. Chem. Soc.* **2010**, 132 (10), 3484–3495. (b) Bera, T. K.; Song, J.-H.; Freeman, A. J.; Jang, J. I.; Ketterson, J. B.; Kanatzidis, M. G. Soluble Direct-Band-Gap Semiconductors LiAsS2 and NaAsS2: Large Electronic Structure Effects from Weak AsS ... Interactions and Strong Nonlinear Optical Response. *Angew. Chem., Int. Ed.* **2008**, 47, 7828–7832.
- (22) Iyer, A. K.; Cho, J. B.; Byun, H. R.; Waters, M. J.; Hao, S.; Oxley, B. M.; Gopalan, V.; Wolverton, C.; Rondinelli, J. M.; Jang, J. I.; et al. Structure Tuning, Strong Second Harmonic Generation Response, and High Optical Stability of the Polar Semiconductors Na_{1-x}K_xAsQ₂. *J. Am. Chem. Soc.* **2021**, *143* (43), 18204–18215.
- (23) Chung, I.; Song, J.-H.; Jang, J. I.; Freeman, A. J.; Kanatzidis, M. G. $Na_2Ge_2Se_5$: A highly nonlinear optical material. *J. Solid State Chem.* **2012**, *195*, 161–165.
- (24) Haynes, A. S.; Saouma, F. O.; Otieno, C. O.; Clark, D. J.; Shoemaker, D. P.; Jang, J. I.; Kanatzidis, M. G. Phase-Change Behavior and Nonlinear Optical Second and Third Harmonic Generation of the One-Dimensional $K_{(1-x)}Cs_xPSe_6$ and Metastable β -CsPSe $_6$. Chem. Mater. **2015**, 27 (5), 1837–1846.
- (25) Chung, I.; Jang, J. I.; Malliakas, C. D.; Ketterson, J. B.; Kanatzidis, M. G. Strongly Nonlinear Optical Glass Fibers from Noncentrosymmetric Phase-Change Chalcogenide Materials. *J. Am. Chem. Soc.* **2010**, *132* (1), 384–389.
- (26) Iyer, A. K.; He, J.; Xie, H.; Goodling, D.; Chung, D.-Y.; Gopalan, V.; Kanatzidis, M. G. Stabilization of the Polar Structure and Giant Second-Order Nonlinear Response of Single Crystal γ -NaAs_{0.95}Sb_{0.05}Se₂. *Adv. Funct. Mater.* **2023**, 33 (9), 2211969.
- (27) Oxley, B. M.; Cho, J. B.; Iyer, A. K.; Waters, M. J.; He, J.; Smith, N. C.; Wolverton, C.; Gopalan, V.; Rondinelli, J. M.; Jang, J. I.; et al. Heteroanionic Control of Exemplary Second-Harmonic Generation and Phase Matchability in 1D LiAsS_{2-x}Se_x. *J. Am. Chem. Soc.* **2022**, *144* (30), 13903–13912.
- (28) McCarthy, T. J.; Kanatzidis, M. G. Use of molten alkali-metal polythiophosphate fluxes for synthesis at intermediate temperatures. Isolation and structural characterization of $ABiP_2S_7$ (A = K, Rb). *Chem. Mater.* **1993**, *5* (8), 1061–1063.
- (29) Marking, G. A.; Evain, M.; Petricek, V.; Kanatzidis, M. G. New Layered Compounds through Polysulfide Flux Synthesis; $A_2Sn_4S_9(A = K, Rb, Cs)$ Present a New Form of the $[Sn_4S_9]^{2-}$ Network. *J. Solid State Chem.* **1998**, *141* (1), 17–28.
- (30) Hjorth Larsen, A.; Jørgen Mortensen, J.; Blomqvist, J.; Castelli, I. E.; Christensen, R.; Dułak, M.; Friis, J.; Groves, M. N.; Hammer, B.; Hargus, C.; et al. The Atomic Simulation Environment—A Python library for working with atoms. *J. Phys.: Condens. Matter* **2017**, 29, 273002.
- (31) Brant, J. A.; Clark, D. J.; Kim, Y. S.; Jang, J. I.; Weiland, A.; Aitken, J. A. Outstanding Laser Damage Threshold in Li₂MnGeS₄ and Tunable Optical Nonlinearity in Diamond-Like Semiconductors. *Inorg. Chem.* **2015**, *54* (6), 2809–2819.

- (32) Zhang, W.; Yu, H.; Wu, H.; Halasyamani, P. S. Phase-Matching in Nonlinear Optical Compounds: A Materials Perspective. *Chem. Mater.* **2017**, 29 (7), 2655–2668.
- (33) Cammarata, A.; Rondinelli, J. Microscopic interactions governing phase matchability in nonlinear optical materials. *J. Mater. Chem. C* **2016**, *4* (24), 5858–5863.
- (34) Liu, J.-M., Ed. Nonlinear Photonics: Phase Matching; Cambridge University Press, 2022, pp 198–233.
- (35) Dmitriev, V. G.; Gurzadyan, G. G.; Nikogosyan, D. N. Handbook of Nonlinear Optical Crystals; Springer Berlin Heidelberg, 2013
- (36) Pearl, S.; Fastig, S.; Ehrlich, Y.; Lavi, R. Limited efficiency of a silver selenogallate optical parametric oscillator caused by two-photon absorption. *Appl. Opt.* **2001**, *40* (15), 2490–2492.
- (37) Zhang, J.-H.; Clark, D. J.; Brant, J. A.; Rosmus, K. A.; Grima, P.; Lekse, J. W.; Jang, J. I.; Aitken, J. A. α-Li₂ZnGeS₄: A Wide-Bandgap Diamond-like Semiconductor with Excellent Balance between Laser-Induced Damage Threshold and Second Harmonic Generation Response. *Chem. Mater.* **2020**, 32 (20), 8947–8955.
- (38) Gallais, L.; Douti, D.-B.; Commandré, M.; Batavičiūtė, G.; Pupka, E.; Ščiuka, M.; Smalakys, L.; Sirutkaitis, V.; Melninkaitis, A. Wavelength dependence of femtosecond laser-induced damage threshold of optical materials. *J. Appl. Phys.* **2015**, *117* (22), 223103.
- (39) Li, R.-A.; Zhou, Z.; Lian, Y.-K.; Jia, F.; Jiang, X.; Tang, M.-C.; Wu, L.-M.; Sun, J.; Chen, L. A₂SnS₃: A Structural Incommensurate Modulation Exhibiting Strong Second-Harmonic Generation and a High Laser-Induced Damage Threshold (A = Ba, Sr). *Angew. Chem., Int. Ed.* **2020**, 59 (29), 11861–11865.